Sensors and Materials, Vol. 38, No. 6 (2026) 3143–3156
MYU Tokyo

S & M 4494

Optimization of Conductive Coatings for Graphite–Carbon Felt Composites in Flow Batteries

Cheng-Hsien Kuo,* Shang-Ching Chuang, and Hung-Yu Chen

Department of Mold and Die Engineering, National Kaohsiung University of Science and Technology, No. 415, Jiangong Rd., Sanmin Dist., Kaohsiung City 807618, Taiwan

(Received February 26, 2026; accepted May 15, 2026)

Keywords: vanadium redox flow battery, electrode, bipolar plate, composite plates, adhesive bonding

The carbon felt electrode contacts the graphite bipolar plate through assembly pressure. The assembly pressure affects the battery's internal resistance. An electrically conductive adhesive (ECA) coating can effectively increase contact area and reduce internal resistance. In this study, a new type of graphite–carbon felt composite plate for a flow battery is proposed. The composite plate comprises three parts: a graphite bipolar plate, a conductive coating, and a hydrophilic carbon felt electrode. These parts can reduce the interfacial resistance between the graphite plate and the carbon felt. The ECA is applied between the graphite plate and the carbon felt to bond them as a whole module. To test the battery module assembled with a conductive coating, the interfacial resistance of the battery assembly and the cell performance were investigated. The optimal bonding parameters were determined using different ECA bonding techniques: coating method (brush painting), adhesive (high-viscosity commercial ECA), and number of coating layers (four). Herein, the conductive coating applied to the graphite–carbon felt composite plate reduces interfacial resistance from 2.15 to 0.85 $\Omega \cdot cm^2$, achieving a >60% reduction and thereby addressing the interfacial resistance between the electrodes (key components of the battery) and the bipolar plate. Moreover, the conductive coating establishes a practical pathway for rapid electron transmission. Several conductive coatings were applied to the flow battery cell for performance testing, and the best performance improvement was achieved with four layers of high-viscosity commercial ECA at a current density of 60 mA/cm^2, yielding a voltage efficiency of 90.4% and an energy efficiency of 81%. Energy efficiency increased by 8.4% compared with the battery without a conductive coating.

1. Introduction

Redox flow batteries are electrochemical energy storage systems designed for large-scale applications. The concept was first introduced in 1974 and has since been developed for use in renewable energy storage due to its scalability, flexible design, and capability for long-duration energy storage. Different types of flow battery have various combinations of two electrolyte-

*Corresponding author: e-mail: chuckkuo@nkust.edu.tw
https://doi.org/10.18494/SAM6306

ISSN 0914-4935

active substances, including all-vanadium, iron/chromium, vanadium/bromine, zinc/bromine, and zinc/nickel. Among them, the vanadium redox flow batteries (VRFBs) are the most mature and widely studied.[1–5] The standard open-circuit battery potential in the VRFB system is 1.26 V. Furthermore, the redox reactions of vanadium electrolyte $V4^+/V5^+$ and $V2^+/V3^+$ occur at the anode and cathode, respectively.[6–8] The output power of the stack is determined by the number of cells and the reaction area of the electrodes, while the concentration and volume of the electrolyte determine the energy storage capacity. Thus, the battery system is designed separately and independently.[9] In VRFBs, excessive compression of the carbon felt electrode increases electrolyte flow resistance, whereas insufficient assembly pressure elevates interfacial resistance with the graphite bipolar plate, ultimately accelerating battery performance degradation.[10,11] Therefore, reducing the contact resistance between the electrode and the bipolar plate is one of the major issues in improving VRFB performance.

Qian *et al.* applied an electrically conductive adhesive (ECA) between the graphite plate and carbon felt, forming effective conductive pathways during hot pressing, enhancing interfacial contact, and reducing area resistivity by 40%.[12] Lim and Lee developed a carbon fiber/polyethylene composite bipolar plate–carbon felt electrode assembly using local thermoplastic welding and achieved minimal areal specific resistance with 2 wt% carbon black in the composite plate.[13] You *et al.* developed a high-temperature conductive binder for integrated electrode bipolar plates, where a 1:0.5:0.5:0.1 ratio of phenolic resin, graphite, B_4C, and SiO_2 achieved the lowest electrical resistance.[14] Kim *et al.* developed an integrated electrode–bipolar plate assembly using a conductive adhesive film, where carbon nanotube (CNT)-coated films exhibited significantly lower contact resistance than those containing carbon black.[15] Cao *et al.* developed an adhesive conducting layer of polypropylene and carbon felt fiber to connect carbon felts and found that composite bipolar plates exhibited higher contact resistance than flexible graphite plates owing to lower carbon content.[16] The adhesive conducting layer effectively reduced electrode–bipolar plate contact resistance, and in prior studies, electrical resistance and battery performance were evaluated, yet coating techniques and immersion thickness remain unaddressed.

In this study, multiwalled CNT coatings with low (3000 cps) and high (10000 cps) viscosities were used, and ECAs with different weight percentages (2.5, 5, 7.5, and 10 wt%) were applied between the graphite plate and the carbon felt. Furthermore, the ECAs were dried and cured for bonding. Then, carbon felt composite plates were prepared for the experiment to examine the effect of the ECA coating on interfacial resistance and to observe the fracture surface appearance after bonding and the degree of immersion of the ECA on the carbon felt surface. Finally, a charge–discharge cycle test was conducted to examine the effect of the interfacial resistance between the graphite plate and the carbon felt on the cell's performance, voltage efficiency (VE), coulombic efficiency (CE), and energy efficiency (EE) in a flow battery. Unlike previous works, in this study, we systematically varied the viscosity, content, and coating layers of CNT-based ECAs for an integrated graphite–carbon felt plate, linking interfacial resistance and immersion thickness to VRFB efficiency.

2. Experimental Procedure

2.1 Preparation and characteristics of adhesive materials

We employed conductive materials with corrosion and acid resistance, as the circulating electrolyte in the flow battery is a strongly acidic corrosive solution. ECAs of low viscosity (L) and high viscosity (H) were used (Jiaxing Naco New Materials Co., Ltd.), as shown in Table 1. ECAs with different weight percentages were prepared. The weight percentage of samples L1 and H1 was 2.5 wt%; that of L2 and H2 was 5 wt%; that of L3 and H3 was 7.5 wt%; and that of L4 and H4 was 10 wt%, as shown in Table 2. The following calculation formula of the weight percentage of samples was used.

$$wt(\%) = (W_2 - W_1)/W_1 \times 100\% \quad (1)$$

Here, $wt(\%)$ is the weight percentage, W_1 is the initial weight of carbon felt and graphite plate before the ECA is applied, W_2 is the total weight of graphite–carbon felt composite plate after the ECA is used, and $W_2 - W_1$ is the net weight of the ECA.

Table 1
Composition of ECAs.

	Low viscosity (L)	High viscosity (H)
Conductive particles	Multiwalled CNTs: Purity ≥ 90% Diameter = 7–15 nm Length = 6–10 μm	Multiwalled CNTs: Purity ≥ 98% Diameter = 7–15 nm Length = 6–10 μm
Typical properties	Viscosity: 3000 cps Resistance: 0.8 Ω Solid content: 30 % Hardness: 2 H Colloidal behavior: oily and thin, Solvent: dimethylacetamide (DMAC)	Viscosity: 10000 cps Resistance: 0.5 Ω Solid content: 50 % Hardness: 3 H Colloidal behavior: oily and thick Solvent: dimethylacetamide (DMAC)
Coating	Method: titration Number of coating layers: 1, 2, 3, and 4 layers (0.5, 1.0, 1.5, and 2.0 ml)	Method: painting with a brush Number of coating layers: 1, 2, 3, and 4 layers

Table 2
Numbering of samples of ECAs with different weight percentages.

No.	Weight before measurement (g)	Weight after measurement (g)	Net weight of ECA (g)	Weight percentage (%)
L1	6.4551	6.6133	0.1582	2.5
L2	6.4470	6.7697	0.3227	5.0
L3	6.4521	6.9362	0.4841	7.5
L4	6.4327	7.0783	0.6456	10.0
H1	6.4577	6.6197	0.1620	2.5
H2	6.4556	6.7800	0.3244	5.0
H3	6.4599	6.9429	0.4830	7.5
H4	6.4649	7.1110	0.6461	10.0

2.2 Process of bonding graphite–carbon felt composite plate

Before coating, the graphite plates and the carbon felt were used as received from the manufacturer without additional surface treatment. Different application methods were used on the basis of ECA viscosity: L ECA was titrated, and H ECA was applied with a brush, as shown in Fig. 1. Additionally, ECAs with different weight percentages were used. The graphite–carbon felt composite plate was fixed with a 1 N·m torsional force applied to the bolts using a torque wrench, and then dried in a vacuum oven preheated to 120 °C and maintained at this temperature for 30 min to allow the ECA to cure and bond to the plate. Thus, a graphite–carbon felt composite plate with a conductive coating was prepared (Fig. 2).

2.3 Determination of graphite–carbon felt interfacial resistance

In the graphite–carbon felt composite plate, the interfacial resistance R_i between the graphite plate and the carbon felt is defined as $R_i = R_t \times S$, where R_t is the surface resistance on the X–Y plane, and S is the contact area of the sample. The experimental device for measuring interfacial resistance is shown in Fig. 3. To measure the resistance, the voltage difference across two copper

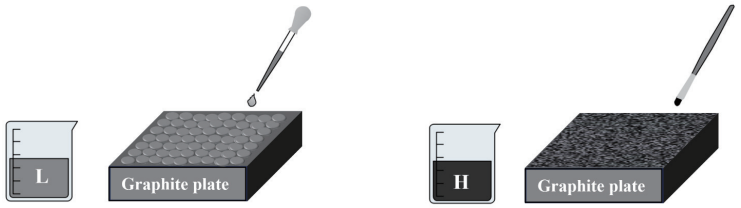

Fig. 1. Coating method of the ECA: (a) titration and (b) painting with a brush.

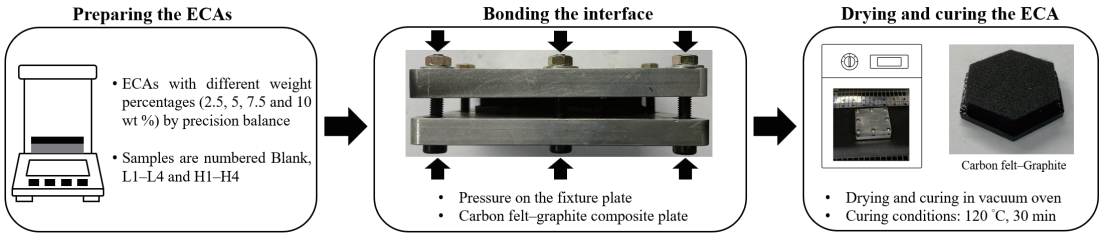

Fig. 2. Bonding procedure of graphite–carbon felt composite plate.

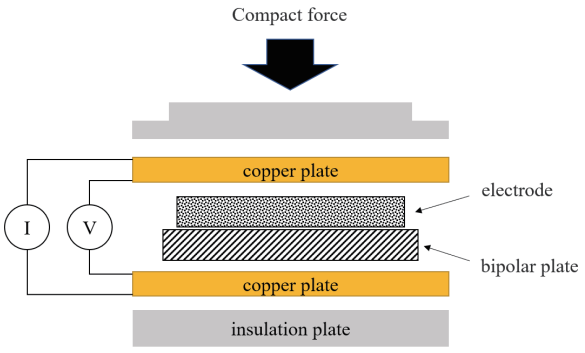

Fig. 3. (Color online) Interfacial resistance measurement.

collector plates sandwiched between the graphite–carbon felt composite plate was measured. However, the voltage difference measured during the test differs from the actual voltage difference; thus, it must be considered that the resistance in the test machine's wiring harness is the short-circuit voltage. Moreover, as the constant current is set to 2 A from the graphite plate to the carbon felt, the resistance on the interface between the two conductors is the interfacial resistance. The sample contact area is 10 cm^2, and the applied pressure is 10 kg, which matches the actual pressure of the battery assembly. The resistance is recorded. The calculation formula for the interfacial resistance of the surface is as follows.

$$\text{Contact voltage drop } (\Delta V) = \text{measured voltage (V)} - \text{short circuit voltage (V)} \quad (2)$$

$$\text{Interfacial resistance } (\Omega \cdot cm^2) = \text{contact voltage drop } (\Delta V) \text{ / current density } (A/cm^2) \quad (3)$$

Here, the contact voltage drop (ΔV) is the actual voltage difference between the two ends of the graphite–carbon felt composite plate after the resistance generated by the wiring harness of the test machine is deducted, and the current density A/cm^2 is the constant current divided by the contact area of the sample.

2.4 Interface structure of materials of graphite–carbon felt composite plate

A stereoscopic microscope (Olympus SZ61, OLYMPUS) was adopted to observe the appearance of the fracture surfaces of samples after adhesive bonding, as shown in Fig. 4, and the samples were then sliced with a precision low-speed saw to check whether the adhesion interface was complete. A scanning electron microscope (S-3000N, HITACHI) was used to observe the cross section of the conductive coating on the carbon felt and to measure the immersion thickness of the ECA. Then, the immersion thickness of the ECA on the surface of carbon felt fibers was compared with the interfacial resistance.

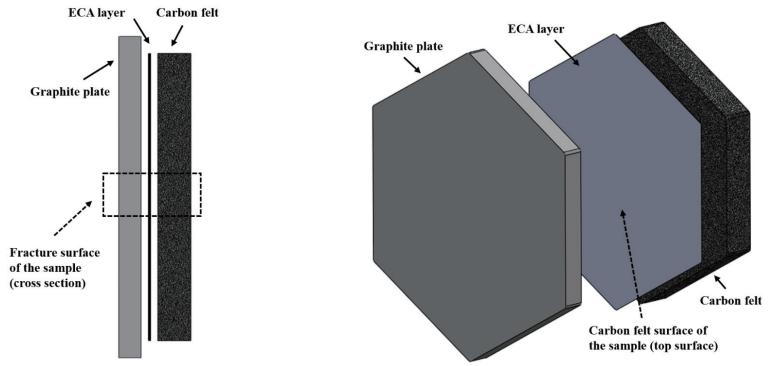

Fig. 4. Observation of ECA bonding: (a) fracture surface and (b) carbon felt surface of the sample.

2.5 Performance of VRFB cell

The VRFB cell experimental device is shown in Fig. 5. The end plate and flow channel frame plate are made of plastic; the sealing washer is made of ethylene-propylene-diene monomer (EPDM) rubber to prevent electrolyte leakage; and the external circulating pipes are made of polytetrafluoroethylene (PTFE). During battery operation, the positive and negative electrolytes are delivered, stored, and supplied through pipelines and a circulation pump, then stored in two barrels outside the battery.[17,18]

To manage the load and power supply, we used a top-notch battery charge/discharge detector (CT-4008-10V10A-NTFA, NEWARE). This device was used for both charging and discharging, enabling us to seamlessly regulate and monitor the battery's operational parameters via the control interface. This ensured automated, continuous maintenance of the charging voltage within the specified range, with an upper limit of 1.6 V and a lower limit of 0.7 V. Charging and discharging performance curves can be used to evaluate the battery's performance. Battery efficiency is evaluated using *CE*, which is the ratio of discharge capacity to charging capacity; *EE*, which is the ratio of discharge energy to charging energy; and *VE*, which is calculated as $VE = EE/CE$.

The charging and discharging parameters used in the experiment are shown in Table 3. As the vanadium electrolyte containing 3.5^{+} vanadium was used at both the positive and negative electrodes, the electrolyte must be precharged before the charging and discharging cycle. In the experiment, the vanadium electrolyte was charged to 1.6 V under a constant current of 1 A, and then charged under a constant voltage of 1.6 V until the current dropped to 0.1 A. Next, it was discharged under a constant current until the voltage dropped to 0.7 V. After the positive and

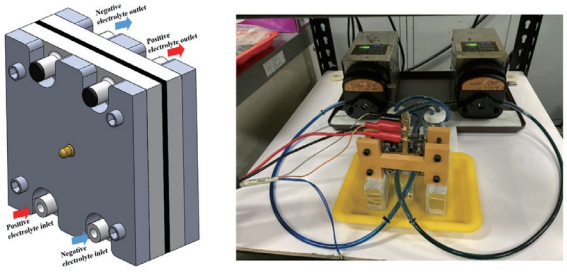

Fig. 5. (Color online) Operating principle and setup of VRFB cell.

Table 3
Conditions of charge–discharge cycle test.

Item	Conditions
Battery test	Cell
Current density	40, 60, 80, 100, 120 mA/cm^2
Voltage range	0.7–1.6 V
Number of cycles	five times under each current density
Proton exchange membrane	GP-IEM-103
Electrolyte volume	30 ml for positive and negative electrodes, respectively
Flow	4.5 ml/min

negative electrolytes were completely separated into vanadium electrolyte containing vanadium of 4^+ and vanadium electrolyte containing vanadium of 3^+, the charge–discharge test can be conducted. The operating conditions are as follows.

(1) Positive and negative electrolytes: 30 ml 1.6 M $VOSO_4$ + 4.6 M H_2SO_4 solution.
(2) Electrode reaction area of positive and negative electrodes: 10 cm^2.
(3) Shape of positive and negative electrodes: regular hexagon.
(4) Flow of circulation pump: ~4.5 ml/min.
(5) Proton exchange membrane: GP-IEM-103 (Liaoning Grepalofu New Energy Co., Ltd.).
(6) All experiments were conducted at room temperature.

3. Results and Discussion

3.1 Effect of ECA on interfacial resistance

After measuring the interfacial resistance, the interfacial resistances of the composite plate coated with the L ECA, the H ECA, and without ECA (blank) were compared, as shown in Table 4. Under a fixed pressure of 10 kg, the interfacial resistances of samples L1–L4 were 1.64, 1.24, 1.10, and 1.02 Ω·cm^2, and those of samples H1–H4 were 1.15, 1.11, 0.96, and 0.85 Ω·cm^2, respectively. The interfacial resistance of L ECA applied by titration changed significantly, whereas that of H ECA applied by brush painting changed little. The blank composite plate with no ECA showed the highest interfacial resistance of 2.15 Ω·cm^2, and the H ECA had a lower interfacial resistance than the H ECA with the same number of coating layers. Hence, the interfacial resistance depends on the content of conductive materials, and the greater the number of coating layers, the lower the interfacial resistance. Here, the lowest interfacial resistance of 0.85 Ω·cm^2 was observed on sample H4, which was reduced by more than 60% compared with that of the blank sample, as shown in Fig. 6. On the basis of the above results, an effective conductive path can be established between the graphite plate and carbon felt by the ECA coating so that electrons can be transported quickly. The interfacial resistance can be effectively reduced.

Table 4
Interfacial resistance measurement data.

No.	Short-circuit voltage (V)	Measured voltage (V)	Net voltage difference (ΔV)	Short-circuit voltage (Ω·cm^2)
Blank	0.0337	0.4627	0.4290	2.15
L1	0.0337	0.3608	0.3271	1.64
L2	0.0337	0.2821	0.2484	1.24
L3	0.0337	0.2576	0.2239	1.12
L4	0.0337	0.2385	0.2048	1.02
H1	0.0341	0.2644	0.2303	1.15
H2	0.0341	0.2536	0.2195	1.10
H3	0.0341	0.2267	0.1926	0.96
H4	0.0341	0.2040	0.1699	0.85

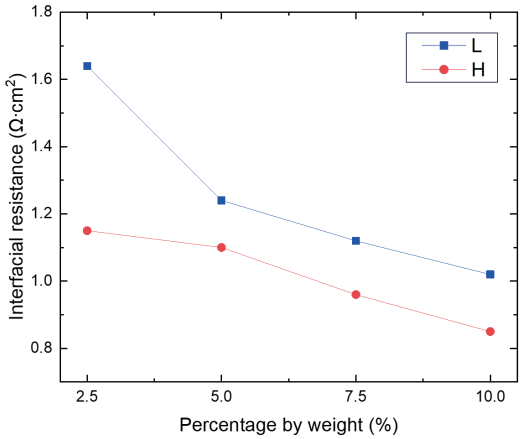

Fig. 6. (Color online) Interfacial resistances of different ECAs (L and H ECAs with 1–4 coating layers) measured at a contact pressure of 10 kg, a contact area of 10 cm², and a constant current of 2 A at room temperature.

3.2 Effect of coating method of ECA on interface structure

After the sample was bonded, we sliced the fracture surface and observed the section, as shown in Fig. 7, with the graphite plate on the left, the carbon felt on the right, and the ECA in the middle. For sample L1, the L ECA at the bonded interface penetrated excessively into the carbon felt, leading to easy peeling from the graphite plate and a sharp increase in interfacial resistance. In contrast, the other samples showed that the ECA properly bonded to the graphite plate and carbon felt, forming strong interfaces. Specifically, L1 suffers from weakened adhesion and peeling at the graphite–carbon felt interface (Fig. 7). In contrast, the H4 sample forms a concentrated, robust bonded layer at the interface owing to its higher solid content and limited penetration. When assembled and cured under a bolt torque of 1 N·m, the H4 composite plate exhibits no observable delamination under an electrolyte flow rate of 4.5 ml/min, indicating that the interfacial adhesion and the clamping force of the cell hardware are sufficient to withstand the hydrodynamic pressure.

Under an external peeling force, the ECA mainly adhered to the surface of the carbon felt fiber, and some ECA remained on the graphite plate. The appearance of the carbon felt surfaces of the damaged samples is shown in Fig. 8. The colloid shows a spherical structure after the L ECA is cured, and a flaky structure after the H ECA is cured. The cured L ECAs exhibit a more spherical morphology. In contrast, the H ECAs form flaky, plate-like domains on the carbon felt surface (Fig. 8). The flaky structure tends to coalesce laterally along the graphite–carbon felt interface, generating continuous CNT-rich layers that bridge neighboring fibers and the graphite substrate, thus providing efficient two-dimensional electron pathways. By contrast, spherical domains form more isolated contact points, forcing electrons to pass through multiple discrete particles and polymer-rich regions, resulting in higher contact resistance.

For the cross section of the carbon felt of damaged samples, Fig. 9 shows the degree of adhesion of the ECA on the surface of the carbon felt fibers and the immersion thickness of the ECA into the carbon felt. A scanning electron microscope was used to measure the immersion

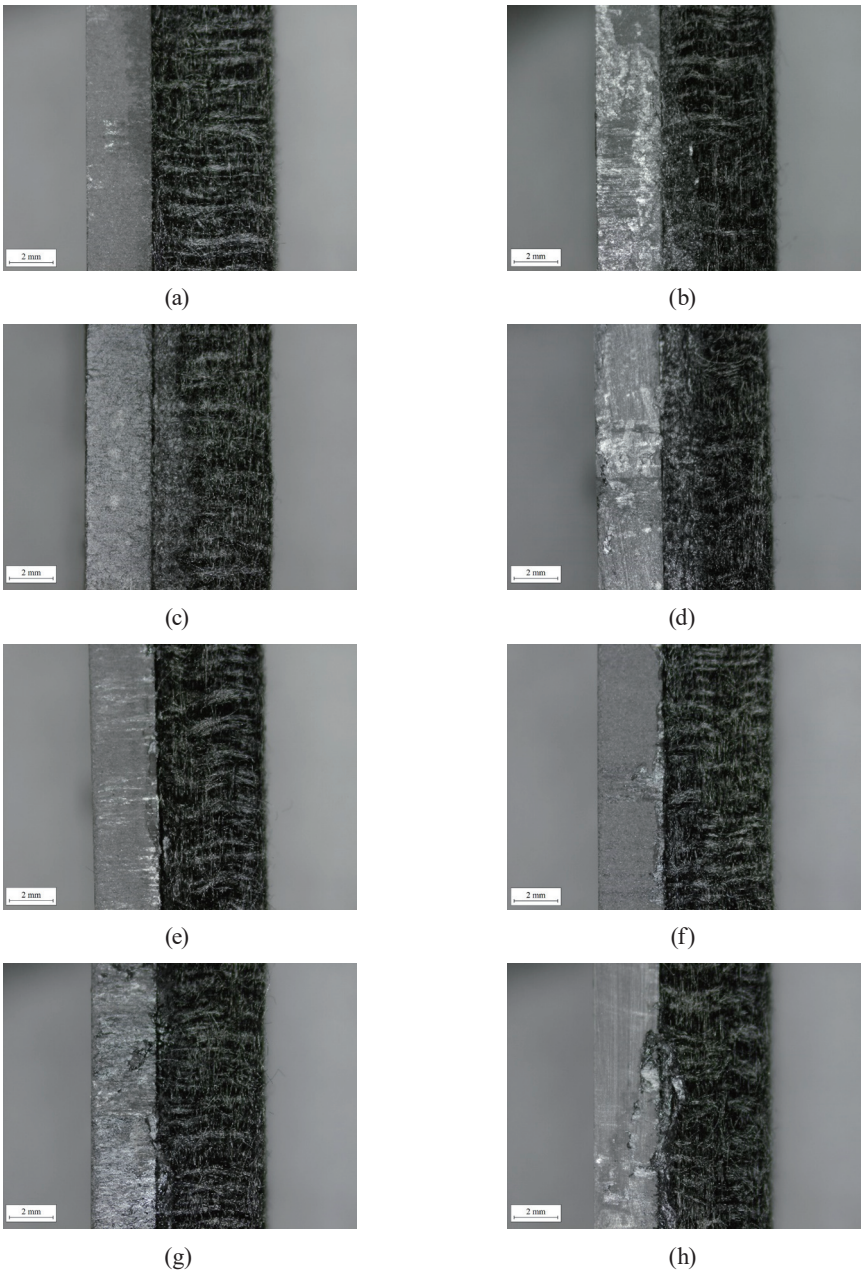

Fig. 7. Fracture surfaces of samples (a)–(d) L1–L4 and (e)–(h) H1–H4.

thickness of the ECA. The immersion thicknesses of the ECA of samples L1–L4 are 190.313, 280.312, 315.000, and 333.750 μm, and those of H1–H4 are 165.938, 170.625, 206.250, and 227.813 μm, respectively. With additional coating layers, the ECA content and immersion thickness increase. At the same time, the interfacial resistance decreases, as shown in Fig. 10. These results indicate that the immersion thickness should not be maximized indiscriminately. In the case of the L ECAs (L1–L4), deeper penetration into the carbon felt increases the risk of

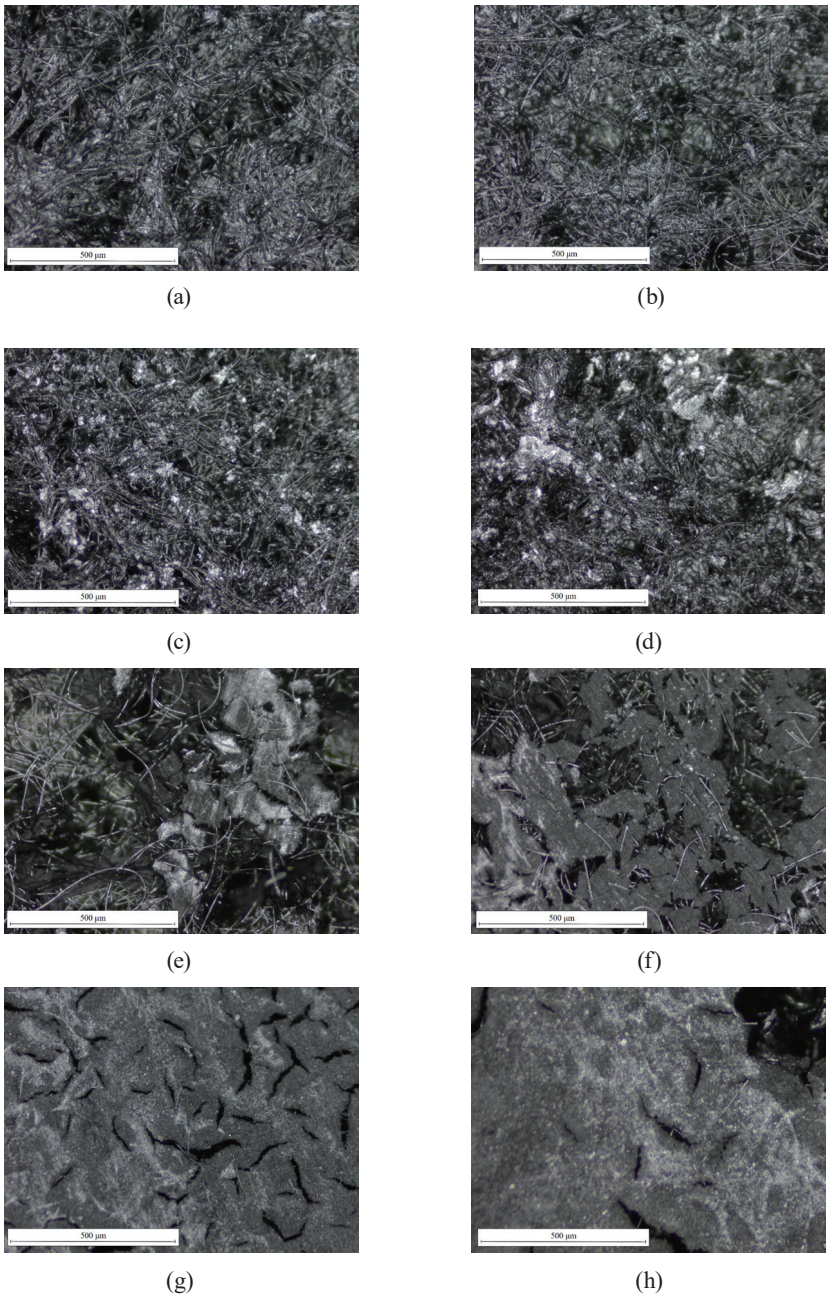

Fig. 8. (Continued) Fracture surfaces of carbon felt of samples (a)–(d) L1–L4 and (e)–(h) H1–H4.

pore blockage and loss of electrochemically active surface area, even as interfacial resistance decreases. By contrast, the H4 sample provides a moderate immersion thickness, the lowest interfacial resistance, and the highest VE and EE, suggesting that only partial filling of the interfacial region is required to establish continuous electronic pathways while maintaining sufficient porosity for electrolyte transport.

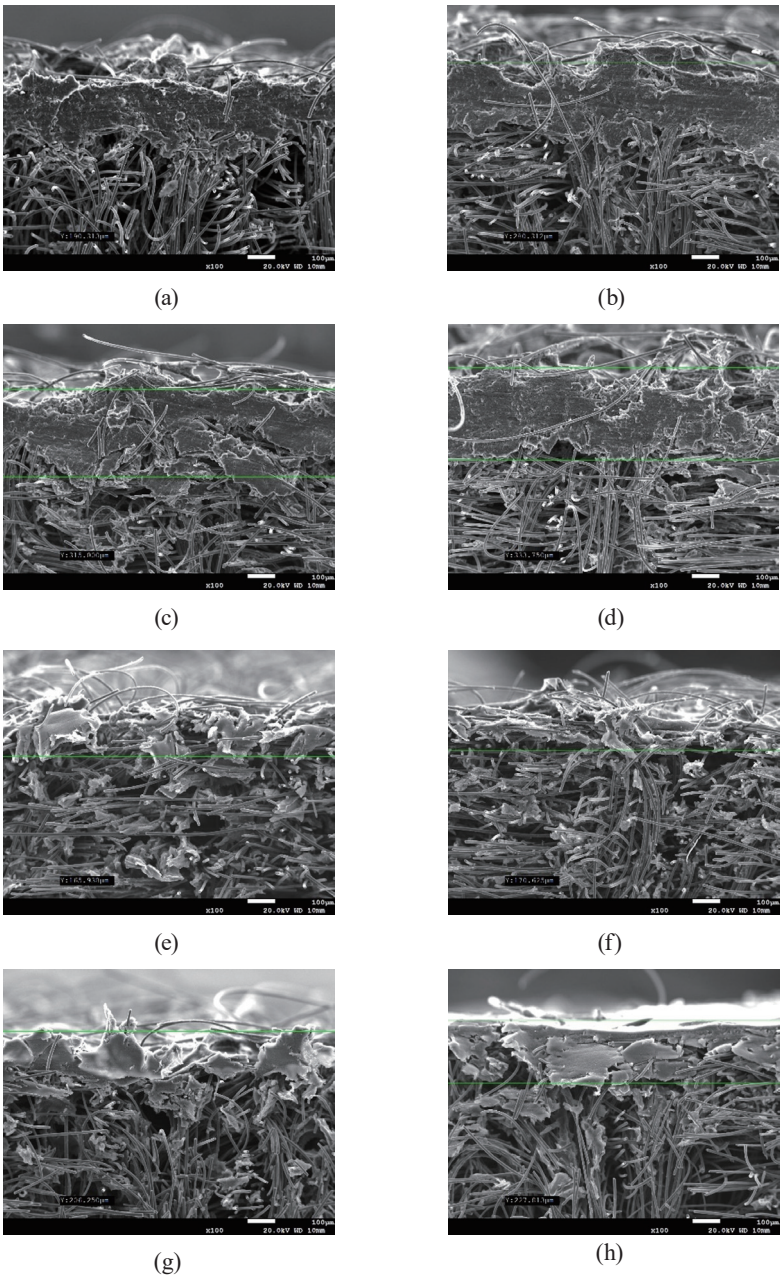

Fig. 9. (Color online) Cross sections of carbon felt of samples (a)–(d) L1–L4 and (e)–(h) H1–H4.

3.3 Effect of ECA on VRFB cell performance

The cell performances are shown in Figs. 11 to 13. The graphite–carbon felt composite plate H4 shows the best conduction, and the VE of sample H4 is obtained to be 93.4, 90.4, and 87.4% under current densities of 40, 60 and 80 mA/cm^2, respectively, making it superior to other experimental samples. Under the current density of 60 mA/cm^2, sample H4 shows a VE of 90.4% and the best EE of 81%, which is 8.4% higher than that of the blank sample. At the current

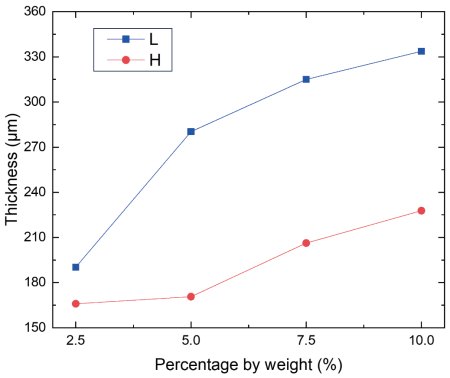

Fig. 10. (Color online) Immersion thickness of the ECA with different coating methods.

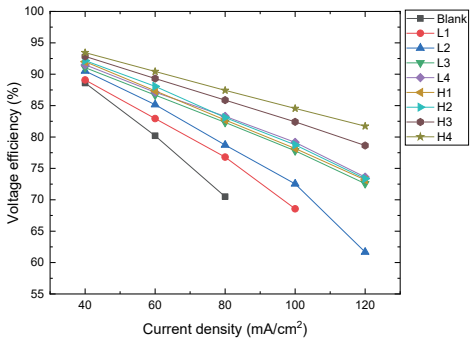

Fig. 11. (Color online) VE of the ECA under different current densities.

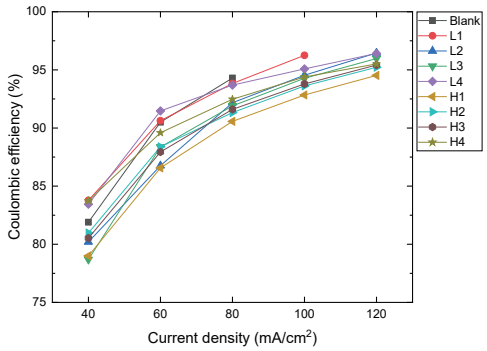

Fig. 12. (Color online) CE of the ECA under different current densities.

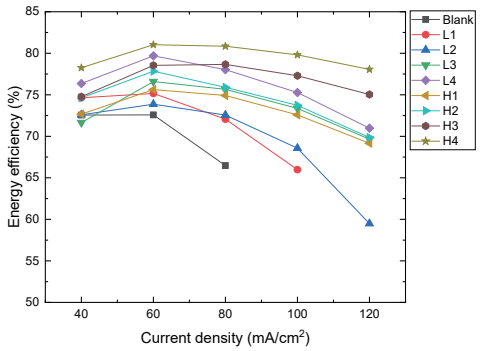

Fig. 13. (Color online) EE of the ECA under different current densities.

density of 120 mA/cm^2, the blank sample and sample L1 exhibit overpotential owing to the very high interfacial resistance, rendering them unable to charge or discharge. However, the VE, CE, and EE of sample H4 can be observed even under high current density and were 81.7, 95.5, and 78.1%, respectively. When the interfacial resistance increases, the VE can be improved, the capacity to carry large currents can be increased, and the polarization caused by the battery's internal resistance can be reduced. On the basis of the above results, the optimal coating condition for sample H4 is an H ECA with 10 wt% solid content, applied in four coating layers onto the graphite–carbon felt interface.

The significant decrease in interfacial resistance from 2.15 to 0.85 Ω·cm² for H4 (Table 4 and Fig. 6) primarily reduces the ohmic IR-drop across the graphite–carbon felt interface. This effect is particularly pronounced at high current density, where the blank and L1 cells fail at 120 mA/cm², while H4 still delivers VE, CE, and EE values of 81.7, 95.5, and 78.1%, respectively (Figs. 11–13). Therefore, the conductive coating mainly mitigates ohmic losses, and any reduction in apparent activation polarization is likely an indirect consequence of the increased effective cell voltage available for the redox reactions. Sample H4 exhibits the lowest interfacial resistance (0.85 Ω·cm²) and the highest VE and EE among all tested conditions. In this work, no apparent

degradation or delamination of the H ECA layer was observed during cycling in 1.6 M $VOSO_4$ + 4.6 M H_2SO_4 electrolyte, suggesting adequate chemical and mechanical integrity of the polymer binder within the tested time window.

4. Conclusions

The optimal bonding parameters were determined by investigating different bonding methods and the application of different ECAs, namely, coating method (brush painting), adhesive (high-viscosity commercial ECA), and number of coating layers (four). The conductive coating applied to the graphite–carbon felt composite plate reduces interfacial resistance from 2.15 to 0.85 Ω cm^2, a reduction of more than 60%, thereby addressing the interfacial resistance between the electrodes (key components of the battery) and the bipolar plate. The conductive coating establishes a practical pathway for rapid electron transmission. Several conductive coatings were applied to the VRFB cell for performance tests, and the best performance improvement was observed with sample H4 at a current density of 60 mA/cm^2, for which VE was 90.4% and EE was 81%. The EE increased by 8.4% compared with that of the blank sample. In the future, the stability of the new graphite–carbon felt composite plate during long-term charge–discharge cycles and the testing of battery cycle life can further demonstrate the potential application of the composite plate assembly in VRFBs.

Acknowledgments

This study was conducted under the industry–academia collaboration project 113A00182, which is supported by ShenEnergy Tech Ltd.

References

1 A. B. Gallo, J. R. Simões-Moreira, H. K. M. Costa, M. M. Santos, and E. M Santos: Renew. Sustain. Energy Rev. **65** (2016) 800. https://doi.org/10.1016/j.rser.2016.07.028
2 R. K. Emmett, and M. E. Roberts: J. Power Sources **506** (2021) 230087. https://doi.org/10.1016/j.jpowsour.2021.230087
3 Z. Huang, A. Mu, L. Wu, and H. Wang: J. Energy Storage **45** (2022) 103526. https://doi.org/10.1016/j.est.2021.103526
4 M. İnci, M. M. Savrun, and Ö. Çelik: J Energy Storage **55** (2022) 105579. https://doi.org/10.1016/j.est.2022.105579
5 Z. Yu, X. Jia, Y. Cai, R. Su, Q. Zhu, T. Zhao, and H. Jiang: Energy Storage Mater. **69** (2024) 103404. https://doi.org/10.1016/j.ensm.2024.103404
6 J. H. Vinco, A. E. E. C. Domingos, D. C. R. Espinosa, J. A. S. Tenório, and M. P. G. Baltazar: J. Energy Storage **43** (2021) 103180. https://doi.org/10.1016/j.est.2021.103180
7 Y. Yao, J. Lei, Y. Shi, F. Ai, and Y. -C. Lu: Nat. Energy **6** (2021) 582. https://doi.org/10.1038/s41560-020-00772-8
8 Z. Zhu, T. Jiang, M. Ali, Y. Meng, Y. Jin, Y. Cui, and W. Chen: Chem. Rev. **122** (2022) 16610. https://doi.org/10.1021/acs.chemrev.2c00289
9 D.-J. Park, K.-S. Jeon, C.-H. Ryu, and G.-J. Hwang: J. Ind. Eng. Chem. **45** (2017) 387. https://doi.org/10.1016/j.jiec.2016.10.007
10 Z. Duan, Z. Qu, Q. Ren, and J. Zhang: Electrochem. Energy Rev. **4** (2021) 718. https://doi.org/10.1007/s41918-021-00108-4

11 R. K. Gautam and A. Kumar: J. Energy Storage **48** (2022) 104003. https://doi.org/10.1016/j.est.2022.104003
12 P. Qian, H. Zhang, J. Chen, Y. Wen, Q. Luo, Z. Liu, D. You, and B. Yi: J. Power Sources **175** (2008) 613. https://doi.org/10.1016/j.jpowsour.2007.09.006
13 J. W. Lim and D. G. Lee: Compos. Struct. **134** (2015) 483. https://doi.org/10.1016/j.compstruct.2015.08.057
14 D. You, J. Lou, and L. Kang: Int. J. Energy Res. **44** (2020) 1920. https://doi.org/10.1002/er.5046
15 M.-Y. Kim, B.-S. Kang, S. -J. Park, J. Lim, Y. Hong, J. -H. Han, and H.-S. Kim: J. Electrochem. Sci. Technol. **12** (2021) 330. https://doi.org/10.33961/jecst.2021.00017
16 J. Cao, T. Luo, J. Zhang, Y. Liu, L. Zhang, J. Li, L. Yang, F. Shen, and J. Sun: J. Energy Storage **97** (2024) 112936. https://doi.org/10.1016/j.est.2024.112936
17 N. Ra and A. Bhattacharjee: Energy Technol. **9** (2020) 1. https://doi.org/10.1002/ente.202000708
18 H. Wang, S.A. Pourmousavi, W.L. Soong, X. Zhang, and N. Ertugrul: J. Energy Storage **58** (2023) 106384. https://doi.org/10.1016/j.est.2022.106384

About the Authors

Cheng-Hsien Kuo received his Ph.D. degree in mechanical engineering from National Yang Ming Chiao Tung University, ROC. He is currently an associate professor in the Department of Mold and Die Engineering at National Kaohsiung University of Science and Technology. His research interests include CAD/CAM/CAE, redox flow batteries, bio-optical sensors, and dissimilar-material joining. (chuckkuo@nkust.edu.tw)

Shang-Ching Chuang received his B.S. and M.S. degrees from National Kaohsiung University of Science and Technology, Taiwan, where he majored in mold and die engineering. He is currently a Ph.D. candidate. His research interests include flow battery systems, bipolar plate welding and sealing technologies, materials engineering, and system integration and sensing for energy applications.

Hung-Yu Chen received his B.S. and M.S. degrees from National Kaohsiung University of Science and Technology, Taiwan, where he majored in mold and die engineering. His research interests include finite element analysis, computational fluid dynamics, materials engineering, and anion exchange membrane (AEM) water electrolysis technology.